

Large blade impeller application for turbulent liquid–liquid and solid–liquid mixing

Giuseppina Montante¹  | Francesco Maluta¹  | Federico Alberini¹  |
Suzuka Iwasawa² | Katsuhide Takenaka² | Alessandro Paglianti¹ 

¹Department of Industrial Chemistry
“Toso Montanari”, University of Bologna,
Bologna, Italy

²Sumitomo Heavy Industries Process
Equipment Co., Saijo, Japan

Correspondence

Giuseppina Montante, Department of
Industrial Chemistry “Toso Montanari”,
University of Bologna, Bologna, Italy.
Email: giuseppina.montante@unibo.it

Funding information

Governo Italiano, “Dipartimenti
eccellenti”, Grant/Award Number:
2018.2023

Abstract

Application of large blade impellers to turbulent single-phase and two-phase mixing is investigated in this work in order to provide a quantitative basis for estimating the possible advantages in industrial mixing operations with respect to fast impeller types. The analysis is based on the discussion of three-dimensional velocity fields collected in a single-phase vessel stirred by a Maxblend impeller by stereoscopic particle image velocimetry and of dispersed phase distribution and liquid mixing time obtained in solid–liquid and liquid–liquid systems by electrical resistance tomography. The results highlight that turbulent two-phase mixing can be efficiently performed in baffled vessels stirred by large blade impellers both in shear-rate controlled and bulk-motion controlled processes.

KEYWORDS

electrical resistance tomography, Maxblend, mixing, stereo-PIV, two-phase flow

1 | INTRODUCTION

Impellers for mechanical agitation of stirred tanks are typically grouped as turbines for low to medium viscosity fluids and close-clearance impellers for high viscosity fluids.^[1] Consequently, for mixing operations under turbulent flow, radial or axial impellers are often selected, while mixing in laminar flow conditions is often carried out by close-clearance impellers. Moving beyond impeller classifications, different impeller types, including both conventional turbines, whose total diameter typically does not exceed half of the tank diameter and the blade axial extension is limited, and large blade impellers, which are characterized by much higher height and diameter, have been recently compared for evaluating the performances in important applications, such as spherical agglomeration of

active pharmaceutical ingredients (APIs), recovery of rare earth minerals by emulsification, and CO₂ hydrate formation for carbon capture. In particular, interesting results were obtained from Chen et al.^[2] in the case of APIs production using a Maxblend (MB) impeller, which gave the least requirement of agitation speed with respect to single and double pitched blade turbines (PBT), both for the solid–liquid and the liquid–liquid operations taking place for accomplishing the agglomeration. Also, higher selectivity in the recovery of minerals by emulsification, most likely associated with higher shear rate uniformity that gives rise to more uniform droplets in the vessel volume, was obtained with an MB impeller with respect to a PBT by Avazpour et al.^[3] Extremely efficient formation of CO₂ hydrates in a tank stirred with an MB impeller with the best energy performance compared with other impeller

This is an open access article under the terms of the [Creative Commons Attribution](https://creativecommons.org/licenses/by/4.0/) License, which permits use, distribution and reproduction in any medium, provided the original work is properly cited.

© 2022 The Authors. The *Canadian Journal of Chemical Engineering* published by Wiley Periodicals LLC on behalf of Canadian Society for Chemical Engineering.

types, probably due to the combination of high pumping capacity, uniform shear field, and good gas–liquid contact, was found by Douïeb et al.^[4]

Besides the above-mentioned examples showing that, depending on the specific design, large blade impellers can provide appropriate flow circulation and good performances in two-phase operations, the hydrodynamics characteristics of these impellers have been investigated in a significantly lower number of cases with respect to traditional fast impellers. Focusing on MB impellers, relatively recent investigations mainly based on computational methods reported good performances from the laminar to the turbulent regime,^[5] the particular shape with a paddle at the bottom surmounted by a grid proved to be very effective for generating efficient mixing at a low-power consumption as compared with other impellers,^[6] effective solid suspension in viscous fluids was obtained with increasing advantages moving towards lower Reynolds numbers from transitional to laminar flows.^[7] On the experimental side, mixing with MB impellers has been characterized by electrical resistance tomography (ERT) in the case of shear-thinning fluid possessing yield stress^[8] and solid–liquid suspensions.^[9] Also, power consumption,^[10] global pumping characteristics,^[11] and mixing time^[12] have been obtained experimentally, mainly with non-Newtonian fluids. The two-dimensional velocity field obtained with MB impellers was also measured by particle image velocimetry (PIV) in Newtonian^[13] and non-Newtonian fluids.^[14]

Given the potential advantages in industrial applications, this work is aimed at discussing the hydrodynamics characteristics obtained with the MB impeller in turbulent single-phase and two-phase flows by a combination of techniques. The original experimental data discussed in the following sections can be used as a basis for the estimation of the suitability of MB type impellers in different turbulent multiphase applications.

2 | MATERIALS AND METHODS

The geometry of the investigated stirred tank is schematically depicted in Figure 1, together with the main components of the instrumentation.

The tank was a Perspex cylinder of diameter, T , equal to 232 mm, with an elliptical-bottom and a total height, H , equal to 355 mm. In the baffled configuration, it was equipped with four baffles of width, W , equal to $T/10$. Agitation was provided with an MB impeller of Standard type (MB-S), of diameter, D , equal to 124 mm and height, H_i , equal to 223.6 mm, placed at the off-bottom clearance of 4 mm.

The physical properties of the fluids adopted in the single-phase and in the two-phase experiments are

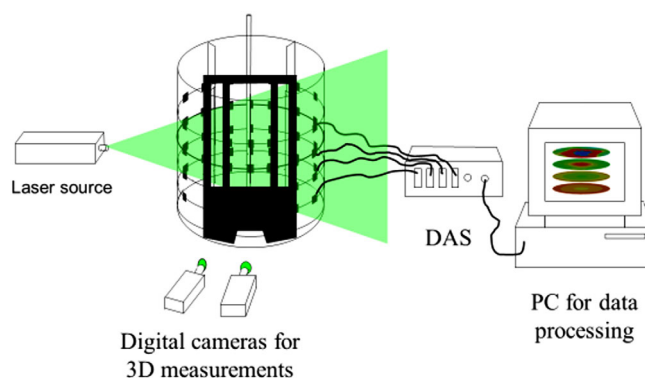


FIGURE 1 Sketch of the stirred tank and instrumentation for particle image velocimetry (PIV) and electrical resistance tomography (ERT). DAS, data acquisition system; PC, personal computer.

summarized in Table 1. The particles were sieved into two narrow size ranges and the mean sizes reported in Table 1 were obtained as the average of the volume-based particle size distributions measured by means of a Malvern Straytec laser diffraction system, which coincide with those already measured by Carletti et al.^[15] All the experiments were carried out at room temperature ($25 \pm 2^\circ\text{C}$) in batch conditions. The impeller speed, N , was varied between 20 and 230 rpm, corresponding to a range of rotational Reynolds number, Re , based on the continuous phase physical properties going from 2.6×10^3 to 6.6×10^4 .

Two experimental techniques have been employed to characterize the mixing performance of the aforementioned mixing vessel for single and multiphase blending configurations. In particular, PIV has been used to measure the velocity field of single-phase systems using water and water/glycerol solutions. ERT has been used to characterize the liquid mixing time in single and two-phase systems and the dispersed phase distribution in liquid–liquid and solid–liquid dispersions.

Different filling ratios were adopted for the different tests. In more detail, the PIV experiments were carried out with two liquid heights, corresponding to the tank diameter ($H_{L1} = 232$ mm) and to 1.2 times the tank diameter ($H_{L2} = 278$ mm). In the ERT experiments, the total filled height was always maintained at H_{L1} .

The impeller performances in single-phase and two-phase conditions are discussed also considering the power consumption characteristics, which are obtained by torque measurements (Kistler torque sensor Type 4501, accuracy class 0.2) in the single-phase vessel filled with water up to H_{L1} . The torque was measured in air before filling the vessel, thus obtaining the torque associated with power consumption due to the bearings and the shaft-motor connections. This value was subtracted from the value measured with the filled vessel to obtain

TABLE 1 Properties of liquids and solids adopted in the investigation

Material	Density, ρ (kg/m ³)	Viscosity, μ (Pa · s)	Mean size, d_p (μm)	Volume fraction, ϕ_d (–)	Experimental technique
Water	997	8.90×10^{-4}	—	—	ERT&PIV
Water/glycerol	1150	8.90×10^{-3}	—	—	PIV
Diesel fuel	826	3.50×10^{-3}	—	0.15–0.40	ERT
Glass ballotini	2450	—	385	0.02–0.12	ERT
Glass ballotini	2450	—	138	0.02–0.10	ERT

Abbreviations: ERT, electrical resistance tomography; d_p , particle size, PIV, particle image velocimetry.

the power consumption, which is the net power transferred to the liquid from the impeller.

2.1 | The stereo-PIV measurements

The instrumentation adopted for the stereoscopic PIV measurements included a Nd:YAG Litron DualPower Laser (light wavelength, $\lambda = 532$ nm, 50 mJ/pulse) and two SpeedSense Lab 340 cameras (2560 × 1600 pixel resolution) fixed on two Scheimpflug mounts. The angle between the cameras was roughly 20°. A Dantec Dynamics system handled the laser control, the laser/camera synchronization, and the data acquisition. The laser light sheet entered the vessel vertically through the tank lateral wall mid-way between two subsequent baffles in the baffled configuration, and the same diametrical plane was investigated also with the unbaffled configuration. The flow was seeded with silver-coated hollow glass particles of a mean diameter equal to 10 μm, and it was illuminated with a light sheet approximately 2 mm thick. The vessel was placed within a larger square vessel made of Perspex filled with the working liquid in order to minimize optical distortion of the laser light. The instantaneous velocity vectors were obtained from the cross-correlation of images collected with the two cameras in double-frame mode. In particular, the analysis of the instantaneous image pairs was carried out through the use of an adaptive-correlation algorithm, applied on interrogation areas (IA) of an initial size of 64 × 64 pixel and a final size of 16 × 16 pixel, allowing the reconstruction of the flow field with a spatial resolution of 1.26 mm. Two validation thresholds, one based on the evaluation of the peak heights in the correlation plane and the other on the velocity magnitude, were adopted. The images from the two cameras were analyzed and validated individually. The data sets collected with the variable position of the impeller blade with respect to the measurement plane were ensemble averaged to obtain a mean velocity field. Finally, the two-dimensional vector fields were combined, using a spatial camera calibration

obtained with a suitable two-level target, into a single ensemble averaged three-component velocity vector field on the planar measurement section, which is depicted in green in Figure 1.

The time interval between the two laser pulses was experimentally set at $\Delta t = 400$ μs for the agitation condition of $N = 80$ rpm, and this value was then proportionally adjusted for all the other rotational speeds considered. The total number of image pairs, which ensured statistical convergence of mean velocities and turbulent fluctuations, was 1000. Based on the approach suggested by Sciacchitano and Wieneke,^[16] the estimated uncertainty in the PIV measurements is equal to 2%–3% of the velocity vector. Additional uncertainty specifically related to Stereo-PIV is in the range of 0.07–0.4 pixel, and the out-of-plane displacement components are affected by 2–3 times larger uncertainties.^[17] As a result, the maximum uncertainty due to the Stereo-PIV configuration of our system corresponds to 0.0945 mm.

In the following sections, a cylindrical coordinate system is adopted, with r , z , and θ being the radial, axial, and angular coordinates, respectively. The origin of the cylindrical coordinate system is placed at the centre of the tank at the axial elevation corresponding to the upper part of the paddle. The mean radial velocity, V , is positive if directed toward the vessel wall; the mean axial velocity, U , is positive if directed upwards; and the mean tangential velocity, W , is positive in the clockwise angular direction, which coincides with the impeller rotation direction.

2.2 | The ERT measurements

The measurements were performed using the ITS 2000 ERT instrumentation (Industrial Tomography Systems Ltd.), which was already adopted for the dispersed phase concentration distribution and the liquid mixing time measurements in two-phase vessels stirred with fast impellers (e.g., in the work of Paglianti et al.^[18]). The measurements were based on the injection of electric current from an adjacent electrode pair at a time and on the

measurement of the voltage difference from the remaining pairs of electrodes. The voltage difference was measured by the circular adjacent strategy.^[19] The local conductivity was obtained from the voltage measurements in real time by the linearized (non-iterative) modified sensitivity back projection (MSBP) algorithm,^[20] that is implemented in the software p2 + V8 together with the sensitivity back projection. The two algorithms provide practically the same conductivity tomograms for the systems investigated in this work. Both methods are based on the linear back projection (LBP), which is the most widely used image reconstruction method,^[21] since it leads to fast image reconstruction and online monitoring and it has been widely applied for two-phase mixing investigations (e.g., in the study of Mishra and Ein-Mozaffari^[9]). The advantage of moving to more sophisticated offline methods based on sensitivity conjugate gradients methods has never been shown in the field of chemical engineering applications of ERT. The electrodes consisted of square stainless-steel plates of size 20 × 20 mm fixed circumferentially on the vessel wall at four axial elevations, and 16 electrodes per plane were used. The corresponding spatial resolution of the conductivity data was equal to 11.6 mm. The design of the electrodes was performed following the recommendations of Ricard et al.^[22] The axial elevations of the four planes, in the following z_1 , z_2 , z_3 , and z_4 , with respect to the bottom of the cylindrical part of the vessel were 12, 57, 102, and 147 mm, respectively. The electrodes were connected to the data acquisition system (DAS) by coaxial cables.

ERT can be applied to two-phase flows when a sufficient conductivity difference between the two phases exists.^[23] For this reason, 0.5 g/L of NaCl was added to the conductive phase, which was demineralized water both in the solid-liquid and in the liquid-liquid investigations. The small amount of salt added to the water was assumed not to affect the water's physical properties. The conductivity of the diesel fuel and the solid particles was assumed to be nil. The p2+ system has an injection current range of 0–75 mA, divided into three broad bands (0–1.5, 1.5–15, and 15–75), and it can operate within the frequency range of 75–153.6 kHz (in 12 steps). In this work, the value of the amplitude of the injected current was equal to 15 mA, and the frequency of 9600 Hz was selected to optimize the signal-to-noise ratio (SNR) of the measured voltage outputs, which depends on several variables, including the liquid conductivity, the vessel size, and the vessel material.

The data rate for the experiments performed with four measurement planes was 6.6 frames per second, corresponding to a temporal resolution of 0.15 s.

The accuracy of ERT for the measurements of holdup of the dispersed phase and the mixing time has been discussed among others by Salem et al.^[24] and Montante and Paglianti.^[25] Electronic noise and liquid temperature

variations are the only remarkable sources of ERT measurement uncertainties. The overall experimental error has been estimated by comparing two consecutive acquisitions performed with pure liquid. The maximum local difference measured on the mean value over 500 acquisitions was found to be equal to 0.1%. The number of samples for obtaining statistic independent averaged holdup was fixed at 500 based on the results of preliminary tests performed with a variable number of instantaneous samples. The local reproducibility of the mean conductivity values based on triplicate measurements was greater than 99.9%.

2.2.1 | Steady state measurements

The dispersed phase concentration distribution was determined from the ensemble average of 500 instantaneous dimensionless conductivity measurements collected after the achievement of a steady state distribution of the dispersed phase at the selected impeller speed.

The local conductivity was obtained on a mesh of 11.6 mm square side per plane, leading to 316 local measurements inside each circular tomogram, and a total number of conductivity values, p , equal to 1264 on the four planes. The raw dimensionless local conductivity in the cell i , C_i , was computed as the ratio between the local conductivity measured in the two-phase system and the reference conductivity.

In all cases, the reference measurement for the conductivity field reconstruction was obtained with the vessel filled with water, since, based on previous results^[26] in this way, a physically consistent representation of the two-phase system can be obtained, provided that the electrodes are not immersed and far enough from any layer of nonconductive phase.

The analysis of the performance of the MB impeller in liquid-liquid and solid-liquid systems was based on the dispersed phase distribution measured at increasing impeller speed and on the determination of the corresponding overall mixing index, defined as:

$$MI_{\text{tot}} = \frac{1}{\bar{C}} \sqrt{\frac{\sum_{i=1}^p (C_i - \bar{C})^2}{p-1}} \quad (1)$$

where p is the total number of conductivity values in the four measurement planes and \bar{C} is the mean dimensionless conductivity on the four planes. The adoption of MI_{tot} was selected due to the expected axial particle/droplet concentration gradients with the Maxlend impeller being more pronounced than the radial ones.^[9] Indeed, the MI_{tot} defined in Equation (1) was found suitable for

taking into account both the axial and the radial gradients of the dispersed phase by Carletti et al.,^[15] where different mixing indexes were compared, specifically those proposed by Harrison et al.^[27] and Hosseini et al.^[28]

2.2.2 | Transient experiments

For the liquid mixing time estimation, the time evolution of the conductivity on the four horizontal vessel sections after the instantaneous injection of a conductive tracer was determined. A small amount of saturated aqueous solution of sodium chloride (0.25 ml for 1 L of mixture) was rapidly injected at the top of the liquid free surface close to the wall approximately midway between two baffles after the achievement of a steady state distribution of the dispersed phase at the selected impeller speed. The measured variable is the raw dimensionless conductivity in the cell i , $C_i(t)$, that is the local conductivity of the liquid at the generic time t , divided by the conductivity of the medium before the tracer injection. As a difference with the case of fast impellers, the experimental time traces obtained with the Maxblend showed a cyclic variation that is clearly related to the blade movements and that required an appropriate data post-processing procedure for the mixing time estimation. It is worth observing that the removal of the periodic effect of the blade passage was not required in the case of the steady state measurements since a sufficiently high number of instantaneous values were ensemble averaged for obtaining the distribution of the dispersed phase.

Instead, for the analysis of the transient experiments, the following procedure was adopted^[29]:

- Measurement of the liquid conductivity during the tracer homogenization, adopting a reference measurement in the stirred medium before the tracer addition, for obtaining the dimensionless conductivity map over time, $C_i(t)$;
- The removal of the periodic effect due to the impeller passage, based on the Fast Fourier transform (FFT) of the dimensionless conductivity time trace and consequent identification of the characteristic signal frequency, which is filtered out;
- Normalization of the filtered signal, for obtaining the normalized dimensionless conductivity over time, $\chi_i(t)$ defined as:

$$\chi_i(t) = \frac{C_i(t) - C_i(t_{inj})}{C_i(t_{\infty}) - C_i(t_{inj})} \quad (2)$$

where $C_i(t_{inj})$ is the conductivity measured before the tracer addition and $C_i(t_{\infty})$ is the value obtained after the complete homogenization. Therefore, the normalized

dimensionless conductivity is equal to zero at the injection time and is equal to one at the end of the homogenization process, irrespective of the initial and final conductivity values. The liquid mixing time is defined as the time required to reach a level of variation within $\pm(1-x)$ of $\chi_i(\infty)$, x being the desired degree of homogeneity, which in this work is taken to be equal to 0.90.

3 | DISCUSSION

The curves of power number, N_p , in baffled and unbaffled configurations are shown in Figure 2. The N_p values measured in the baffled tank in the lower range of Re agree very well with the results reported by Hidalgo-Millán et al.,^[13] who obtained $N_p = 5.97$ for $Re = 1.8 \times 10^4$. The variations of N_p for the baffled tank suggest that in the investigated range of Re , the flow regime is approaching but has not reached fully developed turbulent flow. Approximate values of N_p in fully turbulent conditions can be assumed to be roughly equal to 5 for the baffled vessel.

The following results are divided into four main sections. In the first section, the single-phase velocity fields that characterize the fluid stirred with the MB impeller using the water and the water/glycerol solution are analyzed. In the following sections, the liquid-liquid dispersion and the solid-liquid suspension features are discussed. Lastly, the variation of the liquid mixing time due to the dispersed phase with respect to the single-phase condition is analyzed. The results are all relevant to the baffled vessel, unless the unbaffled configuration is explicitly mentioned.

3.1 | Turbulent single-phase flow characteristics

The hydrodynamics characteristics obtained with the MB impeller in the single-phase stirred tank are presented as colour maps in the following. The three mean velocity components measured at the impeller speed of 80 rpm with the liquid level H_{L2} are shown in Figure 3A-C.

By comparing the magnitude of the three mean velocity components, it is apparent that the flow is mainly driven in the tangential direction and good recirculation is also provided along the axial direction. Together with the prevailing tangential motion, the fluid is pushed axially downward close to the shaft and upward close to the wall, confirming the good vertical circulation already observed by Hidalgo-Millán et al.^[13] in their angle resolved 2D-PIV measurements. The weakest velocity

component is in the radial direction, with maximum values close to the shaft and to the tank bottom.

The effect of the fill ratio, which is of interest since the MB impeller is often adopted in industrial applications in partially filled stirred tanks with variable liquid levels, is also considered. The velocity maps of the three velocity components measured while reducing the liquid level from H_{L2} to H_{L1} are shown in Figure 4A–C.

The results do not highlight significant differences with respect to the case of H_{L2} at the same impeller speed. A specific investigation to determine the critical impeller submergence ratio^[30] was not performed.

The quantitative comparison of the mean velocities obtained at different impeller rotational speeds and successively normalized with the impeller tip speed, V_{tip} , shown in Figure 5, allows one to estimate if the fully turbulent regime is established in the vessel.

As it can be observed, the mean velocity profiles along the radial coordinate at a fixed elevation of $z/T = 0$

and at 140 rpm exhibit minor differences with respect to 100 rpm, particularly for the axial and radial velocity components, while the dimensionless tangential velocity exhibits variations, especially in the range of $r/T = 0.1$ – 0.2 . Therefore, the well-known scalability of the mean velocities in the turbulent regime is almost achieved at the highest impeller speed of 140 rpm. This observation confirms the conclusions drawn from the power curve shown in Figure 2.

Marked deviations from the normalized early turbulent velocity field are instead visible when adopting a solution of water and glycerol of viscosity 10 times higher than that of water, leading to a rotational Reynolds number equal to $Re = 2.65 \times 10^3$. The velocity maps in Figure 6 show appreciable differences with respect to the maps obtained under the same operating conditions with water (Figure 4).

In order to evaluate the possible advantages of adopting the Maxblend impellers in unbaffled turbulent liquid–liquid or solid–liquid stirred tanks with respect to the baffled configuration, given the significantly lower power demand at the same Re shown in Figure 2, the flow field obtained with and without baffles have been compared. As it can be observed, the velocity maps shown in Figures 4 and 7, that are collected under the same operative conditions, highlight that with the unbaffled configuration, the axial component of the velocity vector is almost entirely suppressed, while both the tangential and the radial ones are extremely incremented with respect to the baffled configuration. Since the axial recirculation is very important for both the solid suspension and the liquid draw-down, it is concluded that the baffled configuration is more suitable for turbulent two-phase applications.

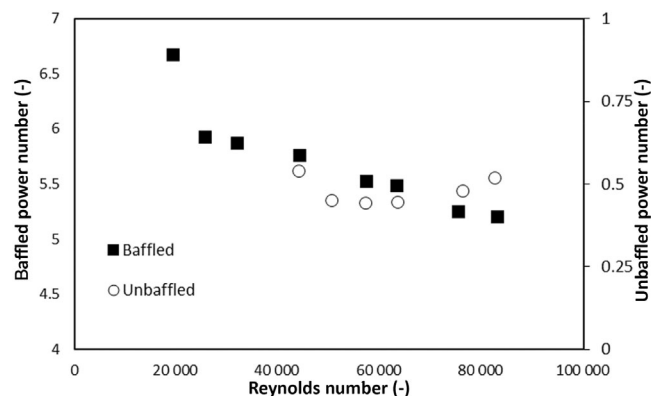


FIGURE 2 Power number for the Maxblend (MB) impeller in the baffled and the unbaffled tank

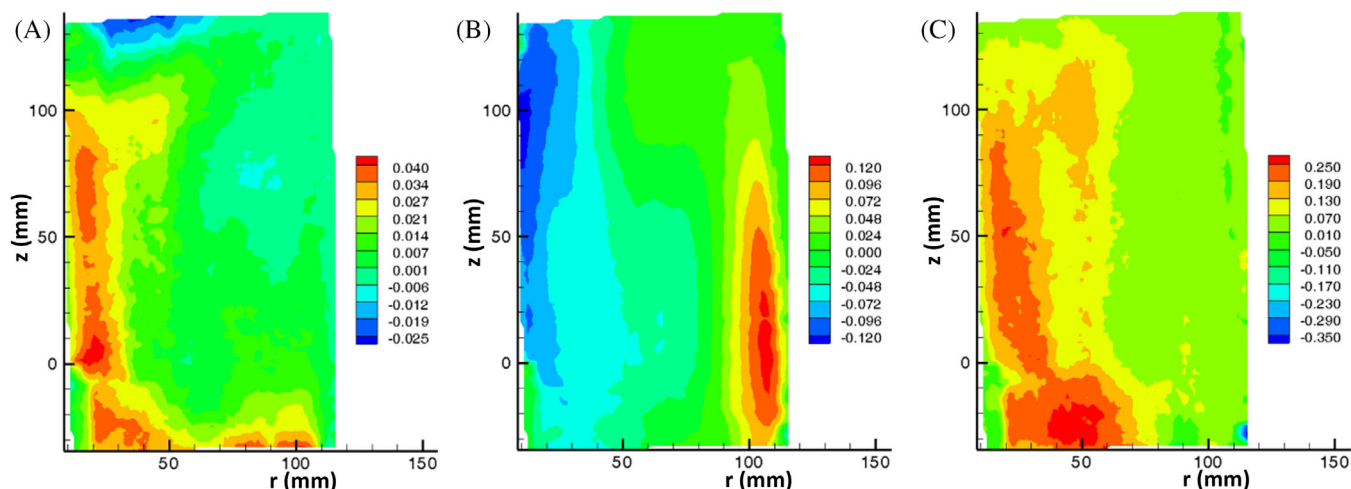


FIGURE 3 Water mean velocity components. $N = 80$ rpm, H_{L2} . (A) Radial velocity V , (B) axial velocity U , and (C) tangential velocity W . The colour scale is in m/s

Finally, the turbulent kinetic energy maps obtained from the axial and radial fluctuating velocity components are depicted in Figure 8.

As it can be observed, the large blade impeller gives rise to almost uniform turbulent characteristics in the vessel volume, which is a significantly different feature with respect to conventional fast impellers (e.g., in the work of Maluta et al.^[31]). As already highlighted, for instance, by Avazpour et al.,^[3] advantages associated to

this aspect can be expected in liquid–liquid dispersion operations, where uniform characteristics of the dispersed phase is often of interest and the size distribution is strictly dependent on the local turbulent field features.

Following the analysis of Stobiac et al.,^[5] the flow generated by the impeller has been further analyzed decomposing it into two parts: the tangential component that follows the rotation of the impeller and the

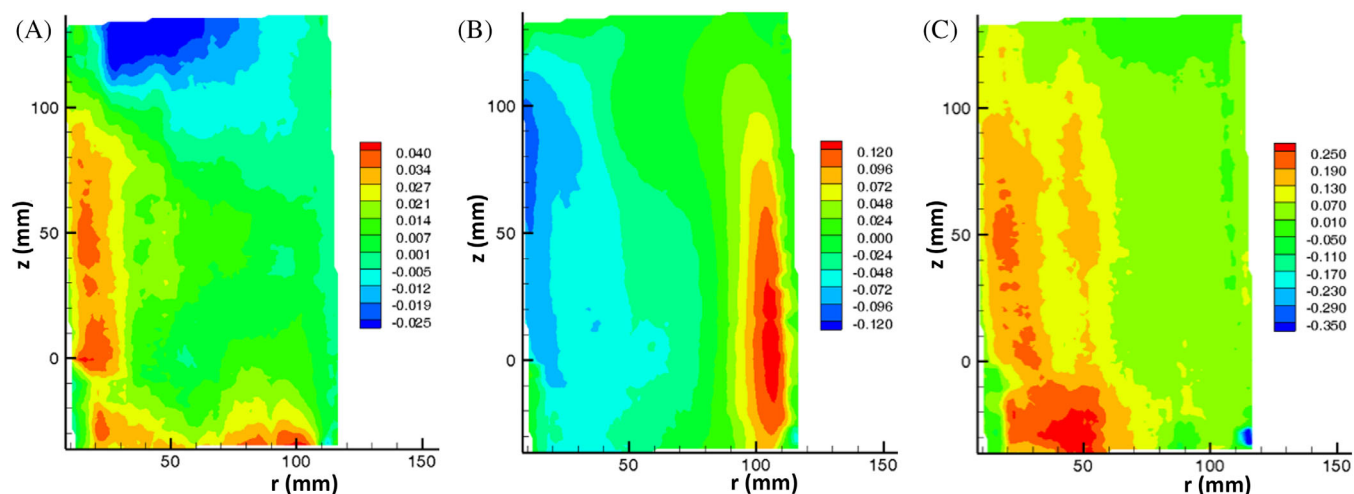


FIGURE 4 Water mean velocity components. $N = 80$ rpm, H_{L1} . (A) Radial velocity V , (B) axial velocity U , and (C) tangential velocity W . The colour scale is in m/s

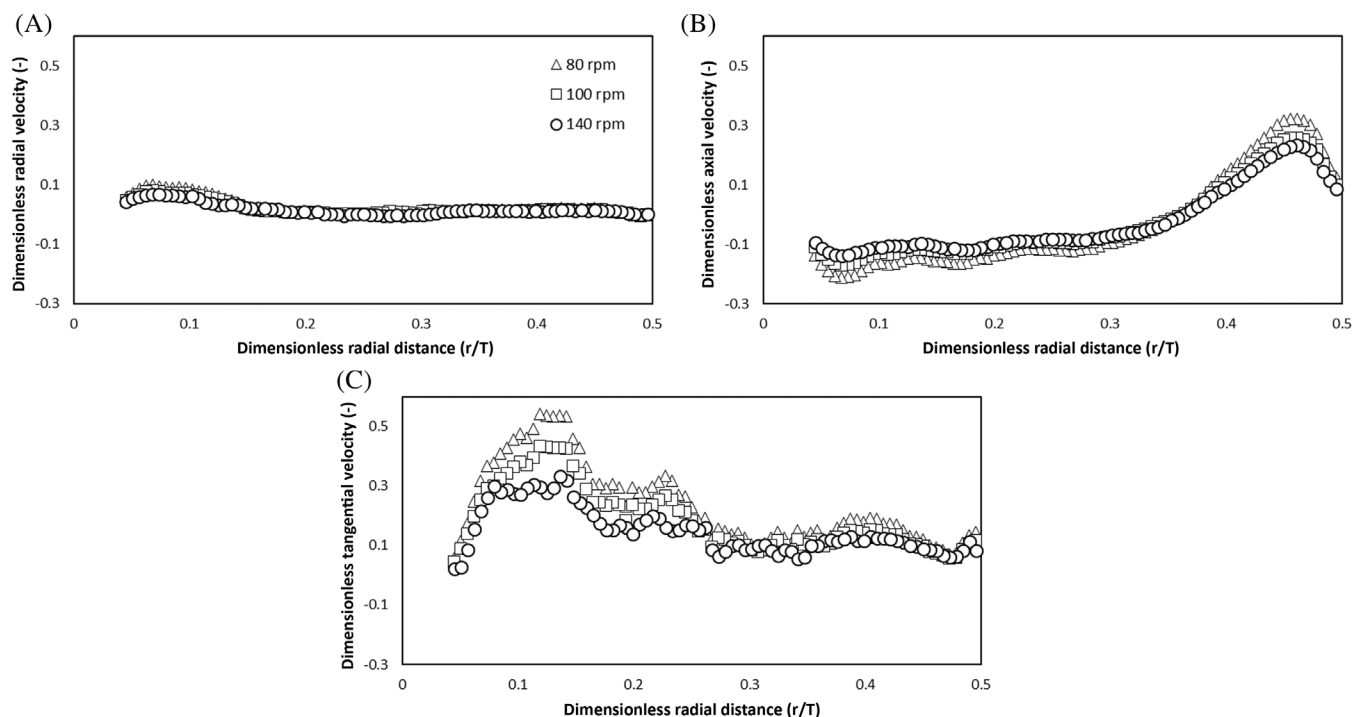


FIGURE 5 Profiles of water mean velocity components normalized with V_{tip} . H_{L1} , $z/T = 0$. (A) Radial velocity V , (B) axial velocity U , and (C) tangential velocity W

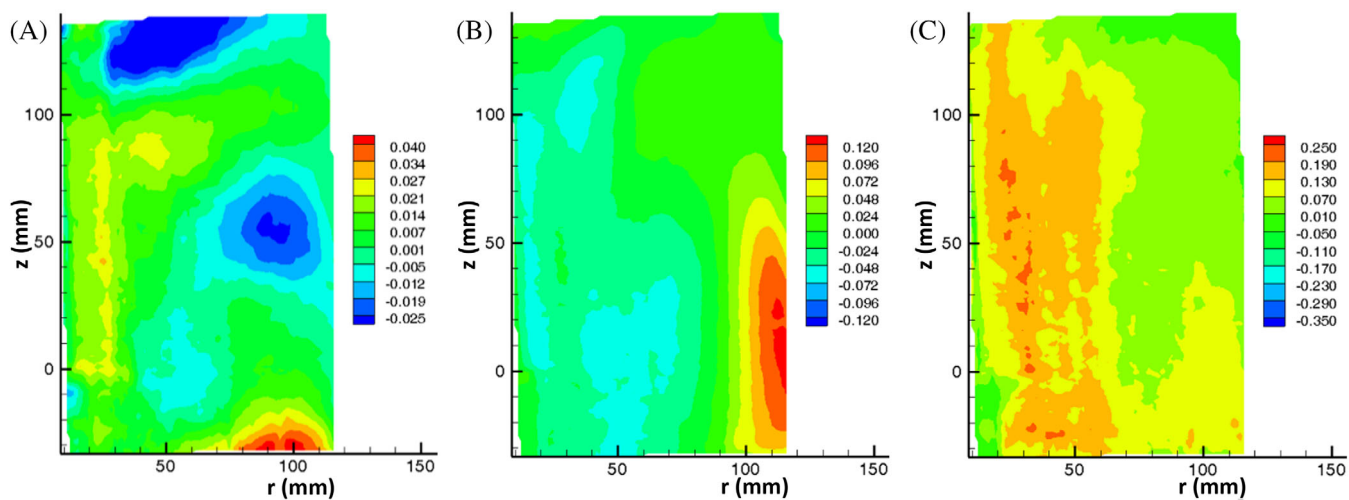


FIGURE 6 Water-glycerol solution mean velocity components. $N = 80$ rpm and H_{L1} . (A) Radial velocity V , (B) axial velocity U , and (C) tangential velocity W . The colour scale is in m/s

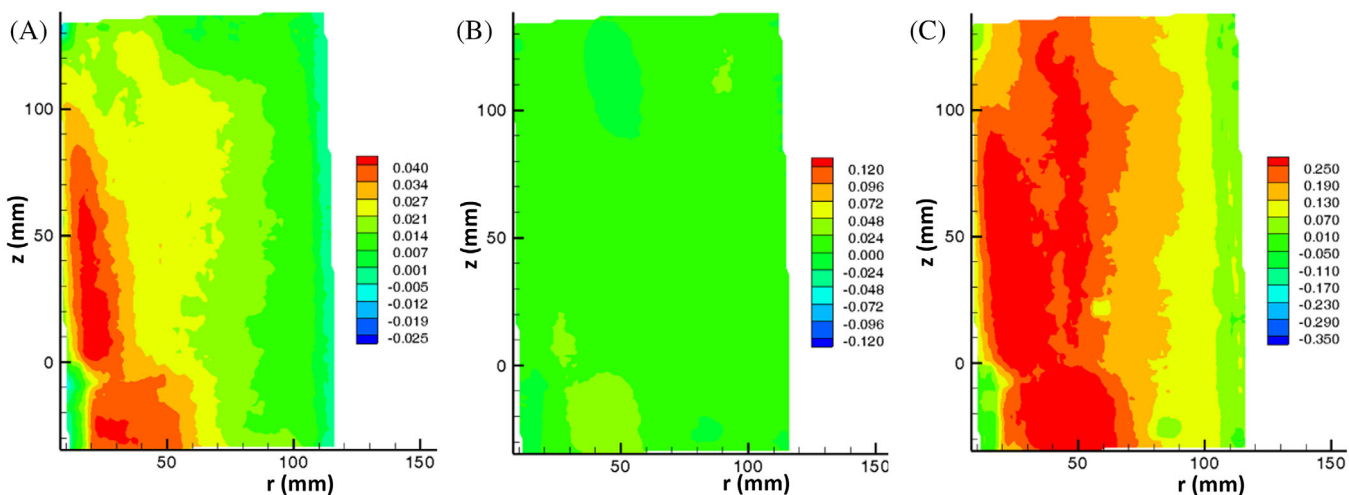
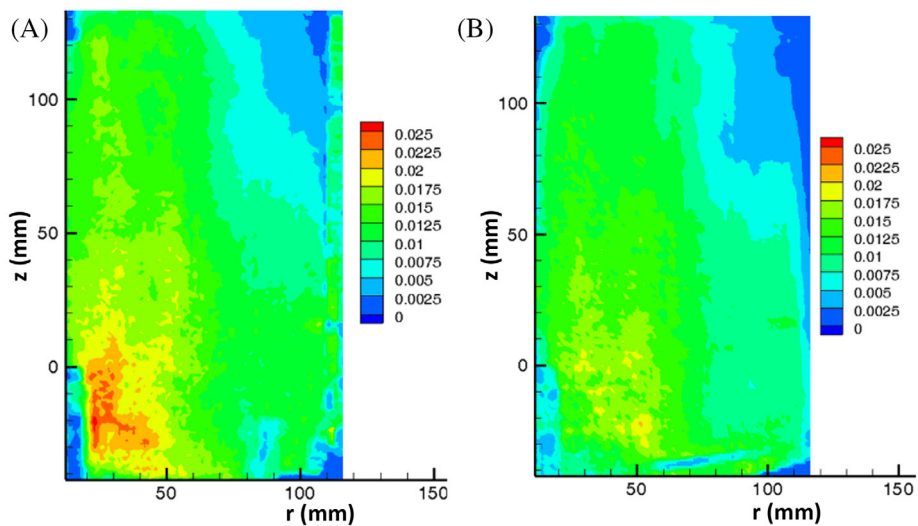


FIGURE 7 Water mean velocity components in the unbaffled vessel. $N = 80$ rpm, H_{L1} . (A) Radial velocity V , (B) axial velocity U , and (C) tangential velocity W . The colour scale is in m/s

FIGURE 8 Turbulent kinetic energy. $N = 80$ rpm, H_{L2} . (A) Water and (B) water-glycerol solution. The colour scale is in m^2/s^2



secondary flow, which is the sum of the axial and radial contributions. The ratio between the secondary flow and the tangential component is shown in Figure 9, highlighting the relative importance of the two contributions.

As expected, the presence of baffles increases the relative importance of the secondary flow that is marked along the axial direction close to the wall, while with the unbaffled configuration (Figure 9C), the secondary flow is practically absent. Moreover, the experimental data evidence that the liquid level influences the flow in the upper part of the tank. Comparing the data collected with two different liquid levels with water (Figure 9A,B) and the water/glycerol solution (Figure 9D,E), it is apparent that the liquid level reduction results in a visible increase in the secondary flow. The increment of the viscosity (Figure 9D,E), irrespective of the liquid level in the tank, induces a reduction of the secondary flow close to the vessel wall.

3.2 | Results in the liquid–liquid system

The performance of the MB impeller in liquid–liquid mixing has been estimated considering the main characteristic regimes, which include:

- The ‘just dispersed’ condition, corresponding to the disappearance of the continuous layer of the light liquid phase from the top of the vessel.
- The ‘completely dispersed’ condition, corresponding to a uniform distribution of the liquid–liquid dispersion in the tank.

In particular, the minimum impeller speed for achieving the completely dispersed condition with different mean volume fractions of the diesel fuel was determined. A quantitative method for this estimation is required because, as a difference between the initial drawdown and the just dispersed condition, the completely

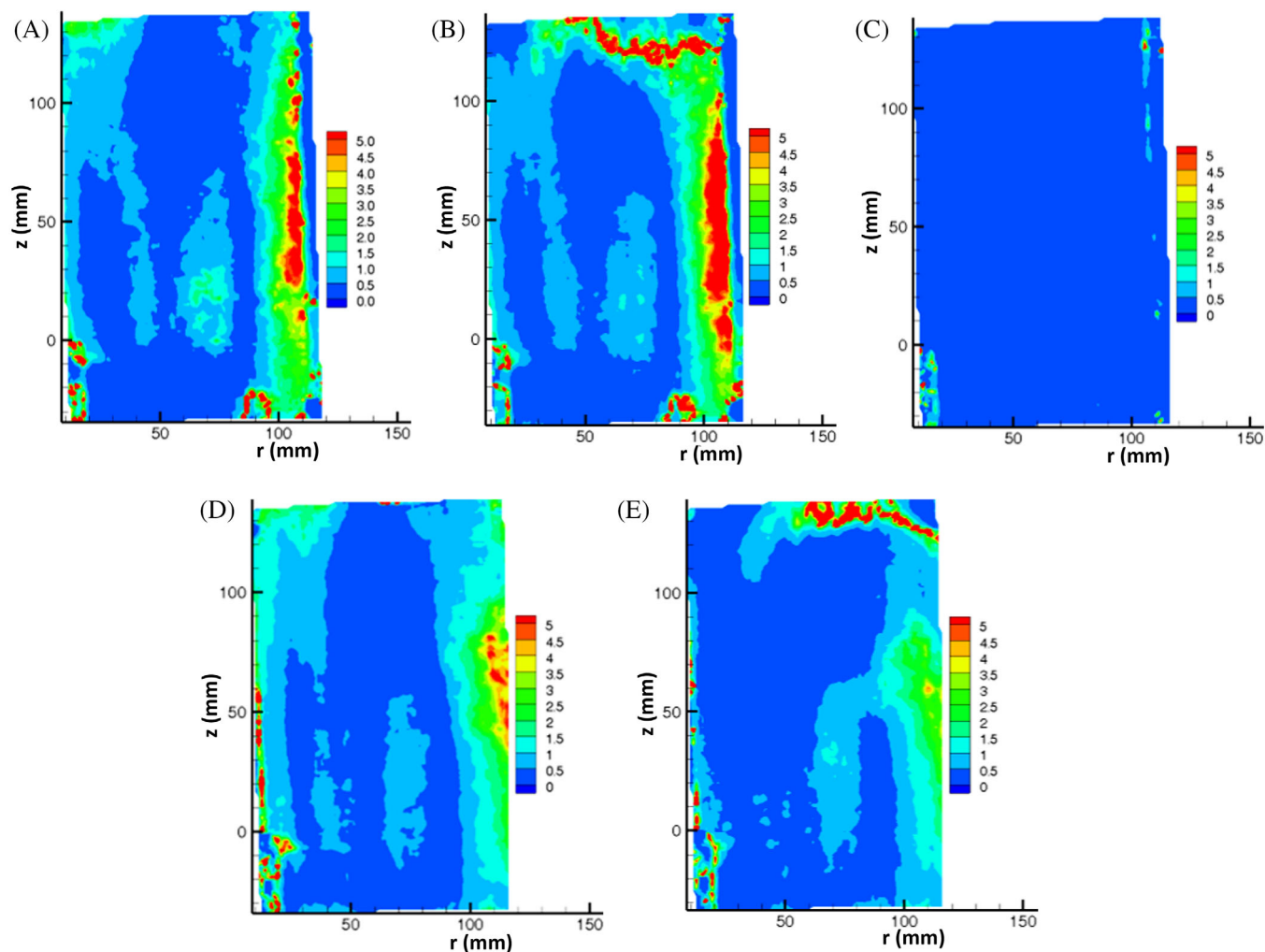


FIGURE 9 Ratio between the magnitude of mean axial and radial velocity and mean tangential velocity: $\frac{\sqrt{u^2+v^2}}{w}$, $N = 80$ rpm, (A) water H_{L2} , (B) water H_{L1} , (C) water unbaffled, (D) water-glycerol solution H_{L2} , and (E) water-glycerol solution H_{L1} . The colour scale is dimensionless

dispersed condition is generally difficult to detect.^[32] Indeed, it cannot be estimated by the visual observation of the tank, even in the simplest case of transparent laboratory stirred tanks. This is why the mixing index analysis is performed using Equation (1) presented in the material and method section. The analysis performed by Maluta et al.^[26] identified a threshold of MI_{tot} to achieve the completely dispersed condition equal to about 0.1.

As can be observed in Figure 10, the MI_{tot} exhibits a continuously decreasing trend starting approximately from 130 rpm. At the highest investigated impeller speed, the values of the MI_{tot} are lower than those obtained with the Rushton turbine in a similar system,^[26] where the drop of MI_{tot} was achieved at about 300 rpm.

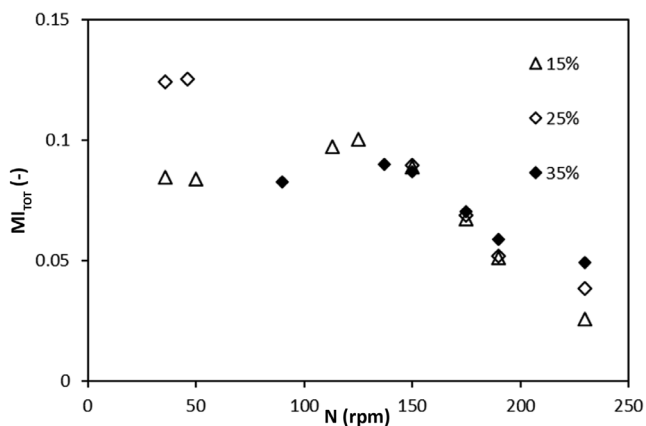


FIGURE 10 Overall mixing index versus impeller speed for different diesel fuel volume fractions

The local distribution of the diesel fluid on the four horizontal sections at different impeller speeds is reported in Figure 11 for $\phi_d = 25\%$. The analysis of the dimensionless conductivity maps confirms the results shown in Figure 10. For $N < 100$ rpm, very low-dimensionless conductivity, which corresponds to high values of dispersed phase volume fraction, is obtained on the upper two planes, while the complete distribution of the dispersed phase is apparent at $N = 150$ rpm, with slight variations at $N = 175$ rpm.

Overall, considering that in the turbulent regime, the MB impeller and the Rushton turbine have similar power numbers, the achievement of complete liquid–liquid distribution at much lower impeller speeds leads us to conclude that the MB impeller is suitable for turbulent liquid–liquid dispersion.

3.3 | Results in the solid–liquid system

Similarly to the case of the liquid–liquid dispersion, the performance of the MB impeller in ensuring adequate solid–liquid mixing, at reasonable energy consumption with respect to other impellers in the turbulent regime, is estimated from the overall mixing index, which is shown in Figure 12A,B, for the 138 and 385 μm particles, respectively. For a sound interpretation of the MI_{tot} , a preliminary determination of the minimum impeller speed for achieving the just suspension condition, N_{js} , was

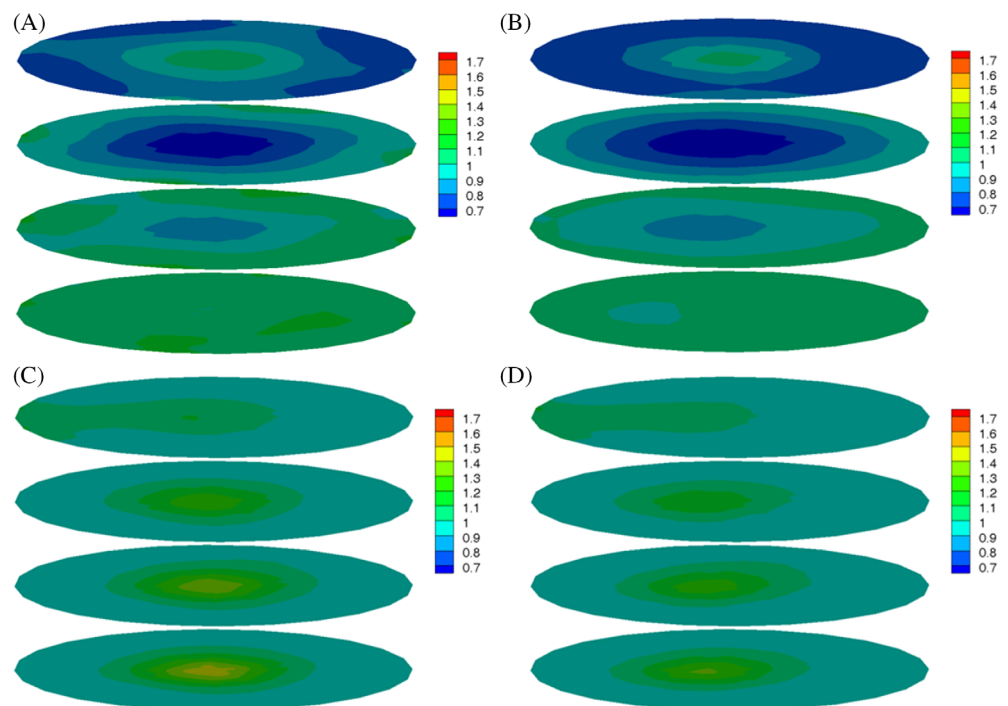


FIGURE 11 Dimensionless conductivity maps on the four measurement sections. $\phi_d = 25\%$. (A) $N = 36$ rpm, (B) $N = 46$ rpm, (C) $N = 150$ rpm, and (D) $N = 175$ rpm

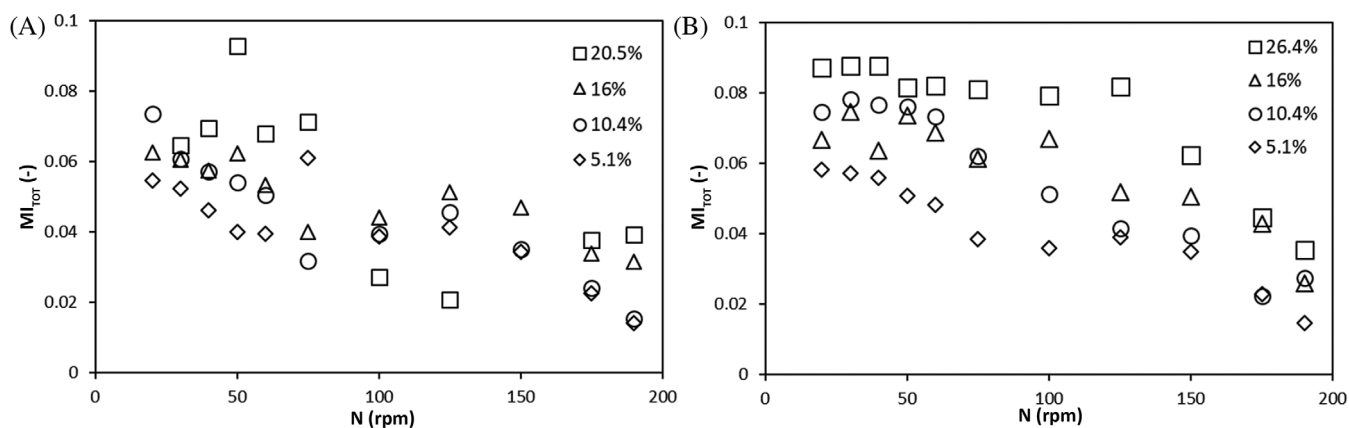


FIGURE 12 Overall mixing index versus impeller speed for different percentage mass ratio of solid particles. (A) $d_p = 138 \mu\text{m}$ and (B) $d_p = 385 \mu\text{m}$

TABLE 2 ‘Just suspended’ impeller speed determined by visual observation of the tank bottom

$d_p = 138 \mu\text{m}$		$d_p = 385 \mu\text{m}$	
X (kg solids/ kg liquid) %	N_{js} (rpm)	X (kg solids/ kg liquid) %	N_{js} (rpm)
5.1	85	5.1	120
10.4	90	10.4	130
16.0	100	16.0	140
20.5	105	20.5	150
		26.4	160

Abbreviations: d_p , particle size, N_{js} , just suspended impeller speed.

performed at the different solid mass ratio, X , and the results are summarized in Table 2.

The experimental data plotted in Figure 12A show that at N less than 100 rpm, large values of the overall mixing index, corresponding to large gradients of the solid concentration, are generally obtained. A definite decrease in MI_{tot} shifted towards greater impeller speeds is apparent also with the bigger particles, as shown in Figure 12B.

As expected, the increase of the impeller speeds above N_{js} leads to an improvement in the solid distribution approaching homogeneous conditions at different values of N depending on the average solid content and the particle size, with a trend that is similar to that obtained by Carletti et al.^[15] with the same particle types and fast impellers, namely, the PBT and the Lightnin A310, that required much higher N values for achieving solid suspension. It is interesting to notice that at N_{js} , the power consumption evaluated with the MB impeller is definitely lower than that evaluated for PBT and Lightnin A310.^[15]

A deeper look into the solid distribution is shown in Figure 13, where the dimensionless conductivity maps measured with the bigger particles and the mass ratio of

20.5% at selected impeller speeds are shown at the four elevations. At low-impeller speed (Figure 13A), both radial and axial gradients of the local solid concentration are noticeable. The gradients decrease as the impeller speed increases, and at $N = 190$ rpm, the distribution of the solid phase is practically homogeneous in the whole tank. It is worth observing that at the lower speed of 100 rpm, that is lower than N_{js} , the solid phase is settled on the tank bottom, and in the centre of the tank, dimensionless conductivities greater than 1 are obtained. That is an experimental error caused by the fact that the z_1 plane is close to the continuous layer of the nonconductive phase. This feature of the ERT measurements was already extensively discussed by Maluta et al.^[26]

A quantitative estimation of the axial differences of solid distribution can be also gained from the comparison of the mean dimensionless conductivity at the four elevations, which are shown in Figure 14 for the same solid–liquid system of Figure 13.

Overall, as also observed with the liquid–liquid dispersion, much lower values of N are required with respect to fast impellers to achieve similar values of mixing indexes and small dispersed phase distribution gradients, as can be noticed comparing the results obtained in this work and in the work by Carletti et al.,^[15] leading to conclude that turbulent two-phase flows are well managed by large blade impellers both in shear-rate controlled and in bulk-motion controlled processes.

3.4 | Liquid mixing time in solid–liquid and liquid–liquid mixtures

In the following section, the effect of the dispersed phase on the liquid mixing time is assessed, considering both the oil droplets and the glass particles in the water. For

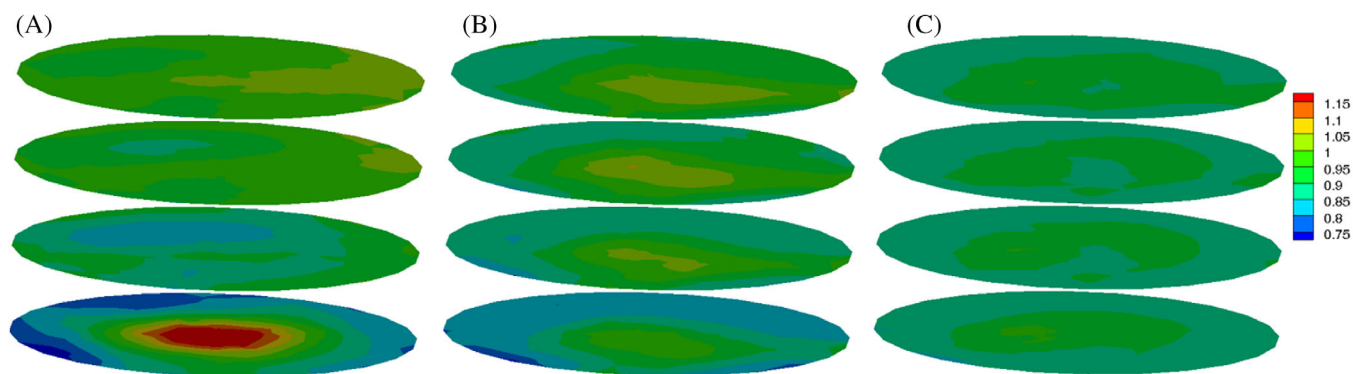


FIGURE 13 Dimensionless conductivity obtained with solid particles ($d_p = 385 \mu\text{m}$, $X = 20.5\%$) in water at different impeller speeds. (A) $N = 100$ rpm, (B) $N = 150$ rpm, and (C) $N = 190$ rpm

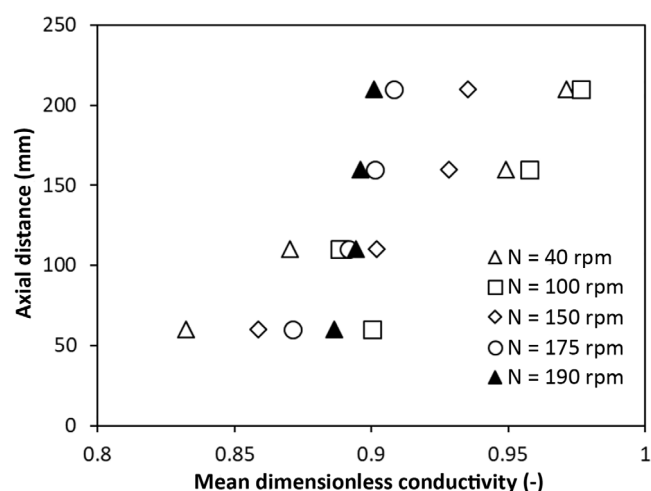


FIGURE 14 Mean dimensionless conductivity on the four measurement sections obtained with solid particles ($d_p = 385 \mu\text{m}$, $X = 20.5\%$) in water at different impeller speeds

the liquid–liquid system, at low impeller speed, the experimental data shown in Figure 15 highlights a clear increment in the time necessary for achieving the 90% homogenization of the tank with respect to the single-phase system, which can be associated with the formation of a stagnant zone of the segregated nonconductive oil phase in the upper part of the tank, where the concentrated salt solution is added. If the impeller speed is greater than the ‘just dispersed’ condition, which in the present case is equal to 120 rpm, the liquid phase is fully dispersed in the tank and the mixing time becomes practically the same as that measured in pure water. The opposite trend is observed with a solid phase added to the tank. If the impeller speed is lower than N_{js} , the solid phase is not fully suspended in the tank and its presence reduces the volume of the tank in which the liquid phase has to be homogenized. Therefore, the measured mixing time appears to be lower than that in pure water. Notably, the mixing time in pure water is consistent with that

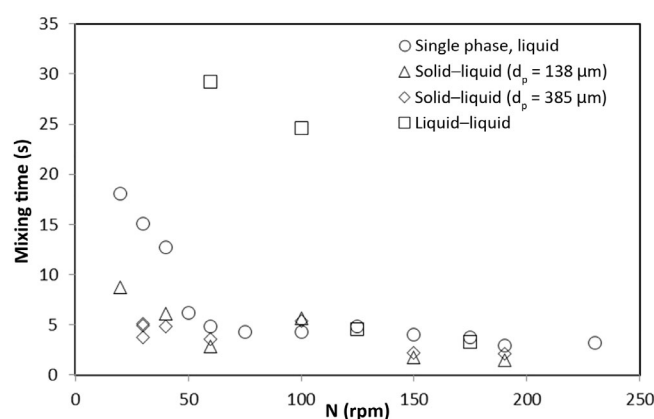


FIGURE 15 Mixing time in turbulent single-phase, solid–liquid ($d_p = 138 \mu\text{m}$, $X = 20.5\%$; $d_p = 385 \mu\text{m}$, $X = 32.4\%$) and liquid–liquid ($\phi_d = 40\%$) systems at different impeller speeds. $H_L = H_{L1}$

reported for non-Newtonian fluids in a similar stirred tank by Fradette et al.^[33] at equal Re . The mixing time measured by decolorization usually corresponds to 99% homogeneity. Applying the usually adopted relationship for reconciling results relevant to different degrees of homogeneity^[34] to the present data, obtained with a homogenization degree of 90%, the dimensionless 99% mixing time of 9 is found in both the investigations at $Re = 2 \times 10^4$.

Mixing time measured at an impeller speed greater than 60 rpm practically equals that measured with pure water. Additional data are required to draw a firm conclusion, but if in fully dispersed liquid–liquid and fully suspended solid–liquid systems, large blade impellers can ensure similar mixing time to the corresponding single-phase system, an advantage with respect to fast impellers might be found. In fact, fast impellers give rise to a much wider variability of mixing time in two-phase flows^[35] and large blade impellers may reduce the process condition uncertainties.

4 | CONCLUSIONS

The three-dimensional velocity fields collected in single-phase conditions with an MB impeller in a laboratory-scale stirred tank provide quantitative evidence of the possible advantages of this impeller type in turbulent multiphase flow applications in baffled tanks. The good balance between homogeneity of the dispersed phase distribution and power consumption with respect to other traditional impellers, both in bulk-motion controlled processes, such as the suspension of solids, and in shear rate-controlled processes, such as the dispersion of immiscible liquids, leads us to conclude that large blade impeller types may be a valid alternative to conventional fast impellers for turbulent multiphase industrial processes.

NOMENCLATURE

Symbols

C_i	local dimensionless conductivity (dimensionless)
\bar{C}	mean dimensionless conductivity (dimensionless)
d_p	particle size (m)
D	impeller diameter (m)
H	vessel height (m)
H_i	impeller height (m)
H_L	liquid height (m)
MI_{tot}	total mixing index (Equation (1)) (dimensionless)
N	impeller speed (s^{-1})
N_p	power number (dimensionless)
N_{js}	just suspended impeller speed (s^{-1})
p	total number of local measurements on the four ERT planes (dimensionless)
t_{inj}	injection time (s)
t_∞	homogenization time (s)
T	tank diameter (m)
U	mean axial velocity (m/s)
V	mean radial velocity (m/s)
V_{tip}	impeller tip speed (m/s)
z	axial coordinate (m)
W	mean tangential velocity (m/s)
x	degree of homogeneity (dimensionless)
X	ratio of weight of solid load on weight of liquid load (dimensionless)

Greek letters

χ	normalized (dimensionless)	dimensionless	conductivity
ϕ_d	volume fraction (dimensionless)		
μ	dynamic viscosity ($\text{Pa} \cdot \text{s}$)		
ρ	density (kg m^{-3})		

Dimensionless numbers

Re rotational Reynolds number ($\rho ND^2/\mu$)

AUTHOR CONTRIBUTIONS

Giuseppina Montante: Conceptualization; data curation; methodology; writing – original draft. **Francesco Maluta:** Conceptualization; data curation; methodology; writing – original draft. **Federico Alberini:** Conceptualization; data curation; methodology; writing – original draft. **Suzuka Iwasawa:** Data curation; investigation. **Katsuhide Take-naka:** Methodology; resources. **Alessandro Paglianti:** Conceptualization; data curation; funding acquisition; methodology; supervision; writing – original draft.

ACKNOWLEDGEMENT

Open Access Funding provided by Universita degli Studi di Bologna within the CRUI-CARE Agreement. Open Access Funding provided by Universita degli Studi di Bologna within the CRUI-CARE Agreement.

FUNDING INFORMATION

The Stereo-PIV instrumentation was funded by the Italian Government through the Grant ‘Excellent Departments’ 2018–2023.

PEER REVIEW

The peer review history for this article is available at <https://publons.com/publon/10.1002/cjce.24483>.


DATA AVAILABILITY STATEMENT

The data that support the findings of this study are available from the corresponding author upon reasonable request.

ORCID

Giuseppina Montante  <https://orcid.org/0000-0001-5075-8010>

Francesco Maluta  <https://orcid.org/0000-0002-0086-1439>

Federico Alberini  <https://orcid.org/0000-0001-8479-6330>

Alessandro Paglianti  <https://orcid.org/0000-0003-3295-9227>

REFERENCES

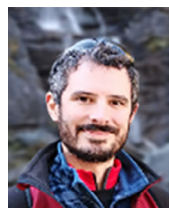
- [1] R. R. Hemrajani, G. B. Tatterson, in *Handbook of Industrial Mixing: Science and Practice* (Eds: E. L. Paul, V. A. Atiemo-Obeng, S. M. Kresta), John Wiley & Sons Inc., Hoboken, NJ **2004**, p. 354.
- [2] C. W. Chen, H. L. Lee, K. L. Yeh, T. Lee, *Ind. Eng. Chem. Res.* **2021**, *60*(30), 11555.
- [3] R. Avazpour, M. Latifi, J. Chaouki, L. Fradette, *J. Environ. Chem. Eng.* **2021**, *9*(4), 105449.
- [4] S. Douïeb, L. Fradette, F. Bertrand, B. Haut, *AIChE J.* **2015**, *61*, 4387.

- [5] V. Stobiac, L. Fradette, P. A. Tanguy, F. Bertrand, *Can. J. Chem. Eng.* **2014**, *92*, 729.
- [6] H. Ameer, *Energy* **2015**, *93*, 1980.
- [7] B. Delacroix, L. Fradette, F. Bertrand, B. Blais, *AIChE J.* **2021**, *67*(11), e17360.
- [8] D. Patel, F. Ein-Mozaffari, M. Mehrvar, *Chem. Eng. Technol.* **2013**, *36*(4), 687.
- [9] P. Mishra, F. Ein-Mozaffari, *Powder Technol.* **2016**, *301*, 701.
- [10] Y. Guntzburger, A. Fontaine, L. Fradette, F. Bertrand, *Chem. Eng. J.* **2013**, *214*, 394.
- [11] Y. Guntzburger, L. Fradette, M. Farhat, M. Héniche, P. A. Tanguy, K. Takenaka, *Asia-Pac. J. Chem. Eng.* **2009**, *4*(5), 528.
- [12] A. Iranshahi, C. Devals, M. Heniche, L. Fradette, P. A. Tanguy, K. Takenaka, *Chem. Eng. Sci.* **2007**, *62*(14), 3641.
- [13] A. Hidalgo-Millán, R. Zenit, C. Palacios, R. Yatomi, H. Horiguchi, P. A. Tanguy, G. Ascanio, *Chem. Eng. Res. Des.* **2012**, *90*(9), 1117.
- [14] A. Fontaine, Y. Guntzburger, F. Bertrand, L. Fradette, M.-C. Heuzey, *Chem. Eng. Res. Des.* **2013**, *91*(1), 7.
- [15] C. Carletti, G. Montante, T. Westerlund, A. Paglianti, *Chem. Eng. Sci.* **2014**, *119*, 53.
- [16] A. Sciacchitano, B. Wieneke, *Meas. Sci. Technol.* **2016**, *27*, 084006.
- [17] A. Sciacchitano, *Meas. Sci. Technol.* **2019**, *30*, 092001.
- [18] A. Paglianti, C. Carletti, A. Busciglio, G. Montante, *Can. J. Chem. Eng.* **2017**, *95*, 1789.
- [19] F. Dickin, M. Wang, *Meas. Sci. Technol.* **1996**, *7*, 247.
- [20] M. Wang, R. Mann, F. J. Dickin, T. Dyakowski, *Proceedings IWISP '96*, Elsevier, Manchester, UK **1996**, p. 647.
- [21] M. Sharifi, B. Young, *Chem. Eng. Res. Des.* **2013**, *91*(9), 1625.
- [22] F. Ricard, C. Brechtelsbauer, Y. Xu, C. Lawrence, D. Thompson, *Can. J. Chem. Eng.* **2005**, *83*, 11.
- [23] S. J. Stanley, *Chem. Eng. Sci.* **2006**, *61*, 7850.
- [24] K. Salem, K. Kling, R. Mann, in *2nd World Congress on Industrial Process Tomography, Proceedings IWISP '96*, International Society for Industrial Process Tomography, Hannover, Germany **2001**, p. 159.
- [25] G. Montante, A. Paglianti, *Chem. Eng. J.* **2015**, *279*, 648.
- [26] F. Maluta, G. Montante, A. Paglianti, *Chem. Eng. Sci.* **2020**, *227*, 115898.
- [27] S. Harrison, R. Stevenson, J. J. Cilliers, *Chem. Eng. Sci.* **2012**, *2012*(71), 392.
- [28] S. Hosseini, D. Patel, F. Ein-Mozaffari, M. Mehrvar, *Chem. Eng. Sci.* **2010**, *65*, 1374.
- [29] S. Iwasawa, H. Kubo, K. Takenaka, S. Pintus, F. Maluta, G. Montante, A. Paglianti, *Chem. Process. Eng.* **2021**, *42*(3), 197.
- [30] S. Motamedvaziri, P. M. Armenante, *Chem. Eng. Sci.* **2012**, *81*, 231.
- [31] F. Maluta, A. Buffo, D. Marchisio, G. Montante, A. Paglianti, M. Vanni, *Int. J. Multiphase Flow* **2021**, *136*, 103547.
- [32] D. A. Brown, P. Jones, J. C. Middleton, G. Papadopoulos, E. B. Arik, in *Handbook of Industrial Mixing: Science and Practice* (Eds: E. L. Paul, V. A. Atiemo-Obeng, S. M. Kresta), John Wiley & Sons Inc., Hoboken, NJ **2004**, p. 145.
- [33] L. Fradette, G. Thomé, P. A. Tanguy, K. Takenaka, *Chem. Eng. Res. Des.* **2007**, *85*(11A), 1514.
- [34] F. Magelli, G. Montante, D. Pinelli, A. Paglianti, *Chem. Eng. Sci.* **2013**, *101*, 712.
- [35] A. Paglianti, C. Carletti, G. Montante, *Chem. Eng. Technol.* **2017**, *40*(5), 862.

AUTHOR BIOGRAPHIES



Giuseppina Montante is a full professor of Chemical Engineering at the University of Bologna. She obtained her PhD from the Università di Palermo in 2000. Her research activity is mainly focused on the development and validation of computational fluid dynamics (CFD) tools for turbulent multiphase and multicomponent systems in industrial chemical equipment. She carried out research activity at the Experimental and Computational Laboratory for the Analysis of Turbulence, King's College London (UK) in the years 1997, 2000, and 2001. The research activity is concerned with the experimental analysis and the modelling of chemical, biochemical, and process industry equipment. She served as an associate editor (2013–2016) and is a member of the International Advisory Board (2017–present) of *The Canadian Journal of Chemical Engineering*.



Francesco Maluta is a junior assistant professor of Chemical Engineering at the University of Bologna in Italy. He received his PhD in Chemical Engineering from the University of Bologna in 2020. Before and during his PhD, he carried out research activities at the University of Alberta, Canada, and at the Toulouse Biotechnology Institute of INSA Toulouse, France. His main expertise is in the numerical simulations of multiphase flows in chemical and process equipment through computational fluid dynamics approaches with open and closed source software. His recent research interests are directed towards the numerical simulations of aerated stirred fermenters and inline separators with a coupled population balance model (PBM) approach.



Federico Alberini is an associate professor of Chemical Engineering at the University of Bologna in Italy. Previously, he was a senior lecturer in the School of Chemical Engineering at the University of Birmingham, UK. He obtained his PhD in Chemical Engineering from the University of Birmingham in 2014. He has been a Chartered Chemical Engineer IChemE since 2021. Specialist topics: fluid dynamic

studies using particle image velocimetry, planar laser-induced fluorescence, positron emission particle tracking, rheology analysis, image processing, passive acoustic, electro resistance tomography, machine learning, and data processing. His current research interests stem from the desire to understand fundamental aspects of process-structure-function relationships in the manufacturing of formulated liquid products with complex rheology.



Suzuka Iwasawa is an engineer at Sumitomo Heavy Industries Process Equipment Co., Ltd. She received a master's degree in Chemistry from Tokyo University of Science in 2019. In the same year, she joined Sumitomo Heavy Industries Process Equipment Co., Ltd. After studying fluid mixing, she carried out research activities on stirred tanks at the University of Bologna, Italy. She then gained experience in designing chemical plants, including distillation towers, from simulation to trial operation.



Katsuhide Takenaka is a technical manager at Sumitomo Heavy Industries Process Equipment Co., Ltd. He received a PhD in Engineering from Yamagata University, Japan, in 1999, and then worked as a lecturer at Yamagata University for a couple of years. He joined Sumitomo Heavy Industries Process Equipment in 2004 after working at a polyurethane company. His major roles in the company are to optimize, propose, and design reactors with agitator for

polymerization and bioreactors. His recent interests are to investigate the cause of fouling, particle agglomeration, and the handling of non-Newtonian fluids.



Alessandro Paglianti is a full professor of Chemical Engineering at the University of Bologna. He earned his PhD in Chemical Engineering in 1993 from the University of Pisa, where he worked as assistant professor and associate professor until 2003. He was honorary research fellow at the University of Birmingham (UK) (1996–1998) and a visiting research fellow at the Institutt for Energiteknikk of Kjeller (Norway) (1991–1992). His main research interests are in the experimental characterization and modelling of multiphase and single-phase equipment, namely, membrane modules, pipelines for two-phase flows, inertial separators, stirred tanks, bioreactors, distillation and absorption columns, fluidized beds, and static mixers. His specific expertise is in the development of experimental methods based on advanced local techniques (PIV, LDA, and ERT) and design models for multiphase flow equipment in industrial plants.

How to cite this article: G. Montante, F. Maluta, F. Alberini, S. Iwasawa, K. Takenaka, A. Paglianti, *Can. J. Chem. Eng.* **2022**, 100(9), 2230. <https://doi.org/10.1002/cjce.24483>